J Adv Ceram

Research Article

Multifunctional ferroelectric heterostructure for high-performance photovoltaic, self-powered photodetection and optoelectronic synapse via non-equilibrium polarization strategy

Guangcheng Wang[1,2,†], Xing Gao[1,2,†], Jianhua Wu[1,2,†], Xin Song[1,2], Shan Zhang[1,2], Ningning Sun[1,2,✉], Pei Han[1,2], Chunxiao Lu[1,2,✉], Liwen Zhang[1,2], Xihong Hao[1,2,✉], Yong Li[1,2,✉]

Cite this article: Wang G, Gao X, Wu J, et al. *J Adv Ceram* 2026, **15**(4): 9221272. https://doi.org/10.26599/JAC.2026.9221272

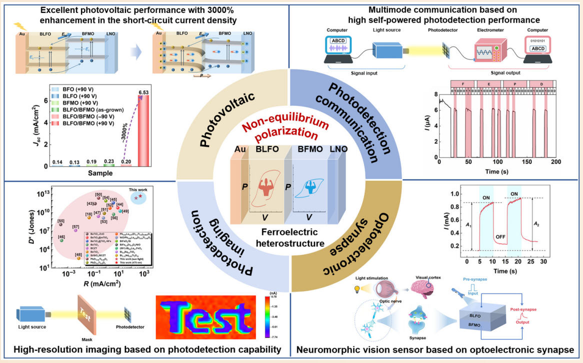

ABSTRACT: Ferroelectrics exhibiting a unique photoelectric conversion mechanism based on spontaneous polarization have attracted significant interest for the development of new optoelectronic devices in the fields of communication, imaging, and sensors. Here, engineering non-equilibrium polarization by constructing a $Bi_{0.9}La_{0.1}FeO_3/BiFe_{0.95}Mn_{0.05}O_3$ (BLFO/BFMO) ferroelectric heterostructure is presented as an innovative strategy for achieving high-efficiency photoelectric responses. Specifically, a 30-fold enhancement in the short-circuit current density is achieved in BLFO/BFMO due to the effective suppression of photogenerated carrier recombination. Benefitting from the high photocurrent density, BLFO/BFMO exhibits superior photodetection performance compared with traditional perovskite ferroelectric-based photodetectors, enabling outstanding dual-mode optical communication and imaging capabilities. Moreover, the non-equilibrium polarization induces an optoelectronic synaptic behavior that is leveraged to implement a neuromorphic vision sensor based on the BLFO/BFMO heterostructure. This work opens a novel route for designing high-performance ferroelectric materials, thereby advancing the development of multifunctional optoelectronic devices.

KEYWORDS: ferroelectric; heterostructure; polarization; thin film

1 Introduction

Vision systems operating in the big data and artificial intelligence (AI) era are expected to simultaneously deliver functional integration, physical miniaturization, and intelligent processing capabilities for handling large-scale visual data [1–5]. In conventional artificial digital vision systems, photoreceptors first capture optical signals from an image and convert them into electrical signals. These signals are then digitized by analog-to-digital converters, stored in memory, and finally processed by a computing unit [6,7]. However, the physical separation of these functional components impedes integration, resulting in high energy consumption and significant signal propagation delays. The key to addressing these challenges lies in developing hardware units that integrate optical sensing, memory, and processing functionalities, specifically, through novel photodetectors and optoelectronic synaptic devices that emulate the human visual system. In this context, ferroelectric materials have attracted considerable interest due to their inherent spontaneous polarization [8,9]. This polarization field can efficiently separate photogenerated carriers and possesses nonvolatile characteristics, providing a unique advantage for constructing optoelectronic devices with integrated functions [8,10–14].

Ferroelectric materials have demonstrated significant progress in detection, synaptic emulation, and sensing applications in recent years [15–19]. Specifically, ferroelectric materials show particular promise for self-powered photodetection, leveraging their unique ferroelectric photovoltaic effect [20–24]. Ferroelectric

---

† Guangcheng Wang, Xing Gao, and Jianhua Wu contributed equally to this work.

[1] Inner Mongolia Key Laboratory of Advanced Ceramic Materials and Devices, School of Materials Science and Engineering, Inner Mongolia University of Science and Technology, Baotou 014010, China. [2] Key Laboratory of Green Extraction and Efficient Utilization of Light Rare-Earth Resources (Inner Mongolia University of Science and Technology), Ministry of Education, Baotou 014010, China.

✉ Corresponding authors. E-mail: N. Sun, sunning@imust.edu.cn; C. Lu, lcx@imust.edu.cn; X. Hao, xhhao@imust.edu.cn; Y. Li, liyong3062545@126.com

Received: December 5, 2025; Revised: February 7, 2026; Accepted: February 24, 2026

https://doi.org/10.26599/JAC.2026.9221272

清華大学出版社 Tsinghua University Press | SciOpen

synapses enable perception-learning capabilities without the need for peripheral electronic components, which establishes a new paradigm for vision sensor technology [15,25]. However, several critical challenges continue to impede the application of ferroelectric materials in visual systems. The inherently low photocurrent density remains a major disadvantage [26,27]. This weak photoelectric conversion capability fundamentally limits the light-sensing performance of ferroelectric materials. Moreover, conventional ferroelectric materials are largely confined to static photoelectric signal conversion, lacking the dynamic and plastic processing capabilities required to emulate synaptic plasticity and other learning behaviors. Consequently, an innovative material design strategy is urgently needed to synergistically enhance the photoresponse efficiency and neuromorphic functionality of ferroelectric materials, enabling the integration of sensing and processing within a single device.

In this work, we propose a non-equilibrium polarization strategy to simultaneously achieve high-performance photodetection and synaptic functionalities based on a $Bi_{0.9}La_{0.1}FeO_3/BiFe_{0.95}Mn_{0.05}O_3$ (BLFO/BFMO) ferroelectric heterostructure thin film. The non-equilibrium polarization between BLFO and BFMO inhibits the recombination of photogenerated electrons and holes, resulting in enhanced dissociation efficiency. Consequently, the BLFO/BFMO heterostructure demonstrates high responsivity and rapid photoresponse under both sunlight and monochromatic light of varying wavelengths, along with precise optical communication and imaging capabilities. Moreover, the non-equilibrium polarization induces a trap state at the interface of BLFO/BFMO, leading to pronounced optoelectronic synaptic behavior under an applied bias. The synaptic behavior enables BLFO/BFMO to exhibit learning and memory functionalities, demonstrating its significant potential as a neuromorphic vision sensor (NVS). This work proposes a new design strategy for ferroelectric materials in optoelectronic applications.

2 Experimental

Sample fabrication: Commercial silicon wafers were used as the substrates in this study. Before film deposition, the substrates were cleaned with deionized water, acetone, and ethanol in turn. The $LaNiO_3$ (LNO) electrode, BLFO, and BFMO films were deposited on Si substrates by a sol–gel method in sequence. For the LNO precursor solution, lanthanum nitrate ($La(NO_3)_3{\cdot}6H_2O$) and nickel acetate ($Ni(CH_3COO)_2{\cdot}4H_2O$) were simultaneously added as precursor salts to 2-methoxyethanol with a La : Ni molar ratio of 1 : 1 under continuous stirring to ensure homogeneous mixing. Spin coating was used to deposit LNO electrodes onto Si substrates at 5000 r/min for 20 s. The as-spin-coated films were dried on a hot plate at 150 °C for 3 min, then baked in a preheated tube furnace at 450 °C, and annealed at 700 °C for 10 min in air using a conventional tube furnace. The spin coating, drying, and baking processes were repeated to prepare LNO films. Finally, the baked LNO films were crystallized at 700 °C for 30 min to form the LNO bottom electrodes. For the $BiFeO_3$-based films, precursor solutions were prepared following a two-step addition procedure. Specifically, for the BFMO precursor solution, $Bi(NO_3)_3{\cdot}5H_2O$ and $Mn(CH_3COO)_2{\cdot}4H_2O$ were first added simultaneously to 2-methoxyethanol. After the solution was completely dissolved, $Fe(NO_3)_3{\cdot}9H_2O$ was subsequently introduced to achieve the designed stoichiometric composition, followed by further heating and stirring to ensure uniformity. A spin coating process was performed at 3000 r/min for 20 s on LNO/Si substrates. The as-spin-coated films were dried on a hot plate at 150 °C for 3 min and then baked in a preheated tube furnace at 300 °C for 10 min in air. The spin coating, drying, and baking processes were repeated to prepare BFMO films. Finally, the BFMO films were crystallized at 500 °C for 30 min. Bismuth nitrate ($Bi(NO_3)_3{\cdot}5H_2O$), iron nitrate ($Fe(NO_3)_3{\cdot}9H_2O$), and lanthanum nitrate ($La(NO_3)_3{\cdot}6H_2O$) were dissolved in 2-methoxy ethanol to prepare the precursor solution of BLFO films. The spin coating and heat treatment processes were the same as those used for BFMO. In addition, the thickness of the films was controlled by the number of spin-coating cycles. The LNO layer was deposited by 10 spin-coating cycles with an average thickness of approximately 25 nm per layer. The BLFO and BFMO layers were deposited by 5 spin-coating cycles with an average thickness of approximately 30 nm per layer.

Characterizations: The crystal structure of the films was determined using a glancing incidence X-ray diffractometer (GI-XRD; Bruker D8 Advance). The cross-sectional microstructure was examined using a field emission scanning electron microscope (FESEM; ZEISS sigma500) and a scanning transmission electron microscope (STEM; Talos F200X G2). X-ray photoelectron spectroscopy (XPS) and ultraviolet photoelectron spectroscopy (UPS) were measured by an X-ray photoelectron spectrometer (Escalab 250 XI). The optical absorption was measured using an ultraviolet–visible (UV–Vis) spectrometer (Hitachi U-4150). The photoluminescence (PL) spectroscopy and time-resolved PL (TRPL) spectroscopy were measured using a fluorescence spectrometer (Edinburgh FLS1000). The domain structure and piezoresponse were analyzed by a piezoelectric force microscope (PFM; Bruker Icon), and the surface potential was measured by a Kelvin probe force microscope (KPFM; Bruker Icon), where the model of the tips is SCM-PIT, which is a silicon probe with a conductive Pt/Ir coating. To measure the photoelectric properties, Au top electrodes with a thickness of 30 nm were sputtered on the surface of the films using a benchtop ion sputtering system (JS-1600, Beijing Hthc Technology Co., Ltd.). The polarization–electric field hysteresis (P–E) loops were measured using a ferroelectric tester (Precision LCⅡ, Radiant Technologies). The films were polarized under a direct current (DC) voltage of +90 V for 200 s, where the Au top electrode was connected to the positive terminal of the power source, while the LNO bottom electrode was connected to the negative terminal. The photoelectric properties were measured using an electrometer (Keithley 2410 and 6517B) under a simulated sunlight source (NBeT, Solar500) and a laser with different wavelengths (NBeT, NBET-LASER). The external quantum efficiency (EQE) was obtained by a spectral response measurement system (Zolix DSR600-NK-JY1). The photocurrent mapping was carried out by a high-precision photocurrent scanning test microscope (HP-PSTM; Mstarter 200).

Density functional theory calculations: The energy band and density of states (DOS) were obtained using density functional theory (DFT) calculations. The calculations were performed using a Vienna *ab initio* simulation package (VASP) within a projector augmented-wave approach. The BLFO and BFMO with an R3c structure were studied using spin-polarized generalized gradient approximation (GGA) with the Perdew–Burke–Ernzerhof exchange-correlation functional. The energy cutoff of the plane waves was 500 eV. A 2 × 4 × 4 Monkhorst–Pack k-points mesh was used for ion relaxations and DOS.

3 Results and discussion

3.1 Material structure and characterization

Figure 1(a) is a schematic illustration of the BLFO/BFMO heterostructure grown on an LNO/Si substrate. The GI-XRD patterns show that BLFO/BFMO exhibits a highly crystalline rhombohedral perovskite structure at various incidence angles (Fig. 1(b)), which is consistent with the individual BLFO and BFMO thin films (Fig. S1(a) in the Electronic Supplementary Materials (ESM)) [28]. The surface atomic force microscopy (AFM) image demonstrates that BLFO/BFMO has a uniform grain size and low surface roughness (Fig. 1(c)). The cross-sectional SEM image of BLFO/BFMO confirms that the heterostructure is composed of two-layer thin films (Fig. 1(d)), and the morphology is similar to that of BLFO and BFMO thin films (Figs. S1(b) and S1(c) in the ESM). A distinct boundary between the BLFO and BFMO layers is clearly observed, with each layer having an approximate thickness of 160 nm. Linear energy dispersive spectroscopy (EDS) confirms the presence of the BLFO and BFMO layers by analyzing the distribution of La and Mn elements (Fig. 1(e)). Following the direction of the red arrows, the relative intensities of La and Mn exhibit notable differences on either side of the boundary. Figure 1(f) shows a cross-sectional TEM image of BLFO/BFMO. High-resolution STEM and selected area electron diffraction (SAED) images confirm that the BLFO layer possesses a rhombohedral perovskite structure (Figs. 1(g) and 1(h)), identical to that of the BFMO layers (Fig. S2 in the ESM). Moreover, high-resolution XPS also verifies that the BLFO and BFMO layers contain La and Mn, respectively (Fig. 1(i)). In addition, the XPS spectrum of O 1s shows that lattice oxygen dominates the oxygen state (Fig. S3 in the ESM) [29]. To verify the ferroelectricity of BLFO/BFMO, PFM is employed to characterize the domain and switching behavior of polarization by writing domains with DC voltages of −18 V/+18 V. Figure 1(j) shows the out-of-plane (OP) phase image, where a distinctly dark and bright square pattern demonstrates a transition from a multi-domain state to a mono-domain state with an opposite polarization direction [30]. The corresponding amplitude map indicates a clear piezoresponse from BLFO/BFMO (Fig. S4 in the ESM). The OP phase/amplitude hysteresis loops demonstrate a strong microscopic ferroelectricity of BLFO/BFMO (Fig. 1(k)). Figure 1(l) shows the polarization–electric field (*P*–*E*) hysteresis loops of BLFO, BFMO, and BLFO/BFMO, confirming robust macroscopic ferroelectricity. Notably, the polarization of BLFO is much higher than that of BFMO. It is worthwhile to consider forming a non-equilibrium polarization state between the BLFO and BFMO layers. In addition, the changes in surface potential before and after poling are investigated. KPFM characterization is performed on the poled and as-grown areas corresponding to the white orthogon in Fig. S5(a) in the ESM. A significant contact potential difference (CPD) is observed between the as-grown and poled areas (Figs. S5(b) and S5(c) in the ESM). This demonstrates that the switching of domain polarization can induce a change in the potential. The high-quality BLFO/BFMO heterostructure and its polarization effect provide a promising platform for research into its photoelectric properties.

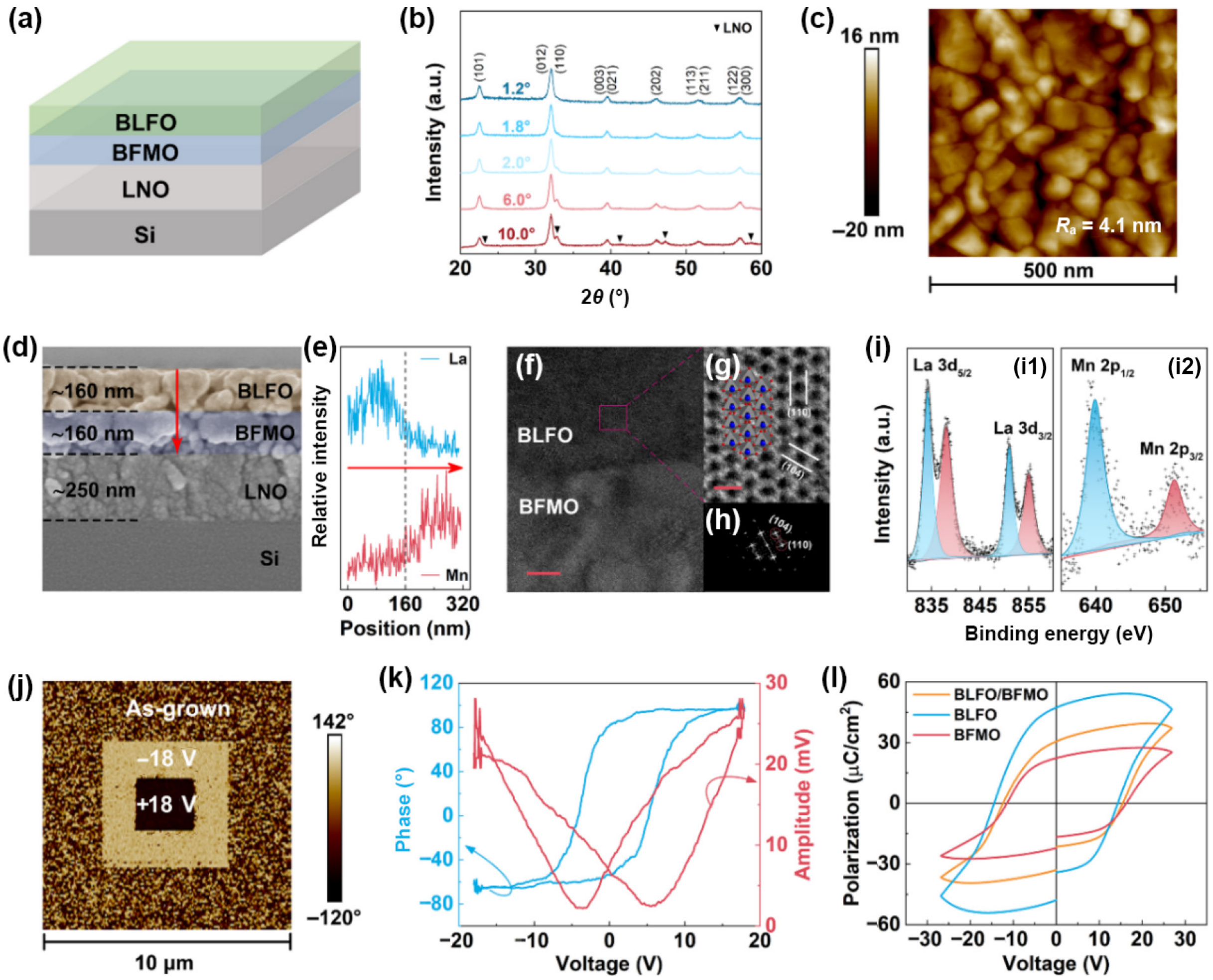

Fig. 1 (a) Schematic illustrations of BLFO/BFMO/LNO/Si. (b) GI-XRD patterns, (c) surface AFM image, and (d) cross-sectional SEM image of BLFO/BFMO. (e) Linear EDS of La and Mn in BLFO/BFMO corresponding to red arrows in (d). (f) Cross-sectional TEM image of BLFO/BFMO. Scale bar: 10 nm. (g) High-resolution STEM image of BLFO layer. Scale bar: 0.5 nm. (h) SAED image corresponding to (g). (i) XPS spectra of La and Mn in BLFO and BFMO layers, respectively. (j) OP phase image of BLFO/BFMO poled by −18 V and +18 V. (k) OP phase and amplitude hysteresis loops of BLFO/BFMO. (l) *P*–*E* loops of BLFO, BFMO, and BLFO/BFMO.

3.2 Photovoltaic performance and mechanism

A vertical Au/BLFO/BFMO/LNO device is constructed to experimentally investigate the photovoltaic performance. Figure 2(a) shows the current density–voltage (*J*–*V*) curves of BLFO/BFMO under 100 mW/cm^2 simulated sunlight. Both the as-grown and poled BLFO/BFMO exhibit a photovoltaic effect, and their photocurrents have the same direction. It is worth noting that the short-circuit current density (J_{sc}) and open-circuit voltage (V_{oc}) after being poled by +90 V (P_{90}-poling) reach 6.53 mA/cm^2 and 0.27 V, respectively. These values are significantly higher than those of the as-grown and −90 V poled (N_{90}-poling) BLFO/BFMO. Moreover, after poling under different voltages, J_{sc} increases with increasing poling voltage, and J_{sc} tends to stabilize when the poling voltage exceeds +90 V, as shown in Fig. 2(b). Therefore, the poling condition has a key effect on the photovoltaic effect of BLFO/BFMO. A comparison of the J_{sc} reveals that the J_{sc} of BLFO/BFMO demonstrates a remarkable advantage, exceeding that of $BiFeO_3$ (BFO), BLFO, and BFMO thin films by more than 3000% (Fig. 2(c)), where the corresponding photovoltaic properties of those thin films are shown in Fig. S6 in the ESM. To explore the mechanism behind the high output photocurrent, the EQE spectra are measured. Compared with BLFO and BFMO (Fig. S7 in the ESM), BLFO/BFMO exhibits a larger EQE (Fig. 2(d)), which is the primary reason for the high photocurrent. The integrated J_{sc} of approximately 6.41 mA/cm^2 obtained from the EQE measurement aligns well with the photovoltaic results. Furthermore, the stability and reliability of BLFO/BFMO are investigated, as shown in Figs. 2(e) and 2(f). The J_{sc} remains nearly constant over a duration of 2000 s, and hardly any degradation is observed when BLFO/BFMO is aged for more than 720 h. Therefore, it is natural to ask what the high photocurrent of BLFO/BFMO originates from.

To probe the origin of the high photocurrent, the electric current–voltage (*I*–*V*) characteristics of BLFO and BLFO/BFMO are compared under the as-grown and P_{90}-poling conditions (Fig. S8 in the ESM). Figure S8(a) in the ESM shows the *I*–*V* curves of both as-grown and P_{90}-poling BLFO in dark and illuminated conditions. The photocurrent (I_P) under various bias voltages is calculated as the difference between the current (I_L) measured under illumination and the current (I_D) in the dark, as shown in Fig. S8(b) in the ESM. It is noted that the *I*–*V* curves of the as-grown BLFO in the dark closely overlap with those under illumination, resulting in a negligible I_P that is nearly zero. Although the I_L for the P90-poling BLFO is greater than that of the as-grown BLFO, its corresponding I_P remains small. In addition, BFMO exhibits a similar I_P behavior to that of BLFO. The *I*–*V* behavior of the as-grown BLFO/BFMO is similar to that of BLFO (Figs. S8(c) and S8(d) in the ESM). However, the I_P of the P_{90}-poling BLFO/BFMO is significantly larger under the same bias voltages. It is known that the photovoltaic effect is closely related to the light absorption and dissociation efficiency of the photogenerated carriers [21]. Owing to the similar absorption behavior of BLFO/BFMO compared with that of BLFO and BFMO (Fig. 3(a)), it is suggested that light absorption is not the dominant factor contributing to the enhanced output photocurrent of BLFO/BFMO. Therefore, it is proposed that the dissociation efficiency of the photogenerated carriers may be the key factor, which is generally determined by the photogenerated-carrier separation and recombination. Based on UPS results of the BLFO and BFMO layers in BLFO/BFMO (Fig. S9 in the ESM), the energy band structure of BLFO/BFMO is obtained, as shown in Fig. 3(b). The driving electric fields for separating photogenerated carriers are primarily the built-in fields (E_{bi}) at the BLFO/BFMO interface and the depolarization fields (E_{dp}) induced by ferroelectric polarization of the BLFO and BFMO layers, as shown in Fig. 3(c). According to the photovoltaic results presented in Fig. 2(a), the as-grown, N_{90}-poling, and P_{90}-poling BLFO/BFMO exhibit the same photocurrent direction, indicating that ferroelectric polarization is insufficient to induce a switchable photovoltaic effect in BLFO/BFMO. It can be concluded that E_{bi} is the primary driving electric field, rather than E_{dp}. More importantly, it can be reasoned that the net driving electric field is

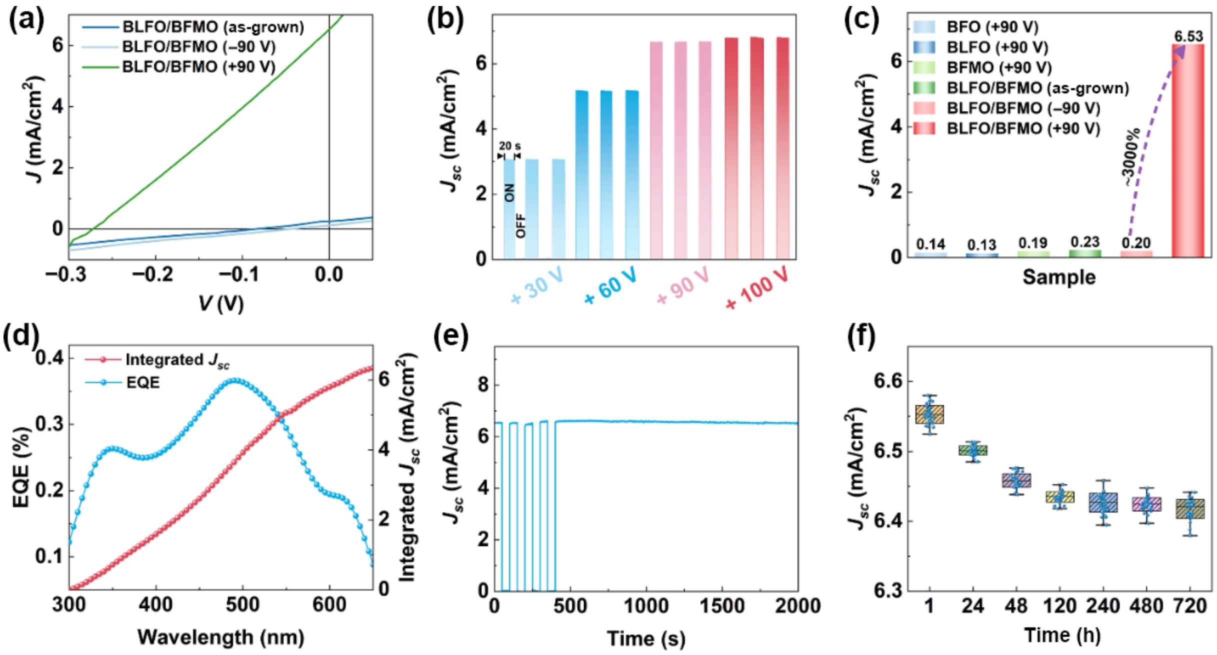

Fig. 2 (a) *J*–*V* curves of as-grown and poled BLFO/BFMO under sunlight of 100 mW/cm^2. (b) Switching response of J_{sc} for BLFO/BFMO after poling with different voltages. (c) Comparison of J_{sc} between BLFO/BFMO and other ferroelectric thin films. (d) EQE and integrated J_{sc} of BLFO/BFMO. (e) Time-dependent J_{sc} of BLFO/BFMO in 2000 s. (f) J_{sc} of BLFO/BFMO aged for over 720 h.

reduced due to the opposing directions of E_{bi} and E_{dp} after P_{90} poling. Nonetheless, its J_{sc} remains significantly larger than that of the as-grown and N_{90}-poling BLFO/BFMO. Additionally, the as-grown BLFO/BFMO exhibits a small I_{P}, even though a large external bias voltage is applied (Figs. S8(c) and 8(d) in the ESM). Therefore, the driving electric field cannot be identified as the determining factor for the high photocurrent either.

By investigating the PL spectroscopy of BLFO, BFMO, and BLFO/BFMO after positive poling, it is found that the PL peak intensity of BLFO/BFMO is lower than that of both BLFO and BFMO (Fig. 3(d)). This result indicates that the recombination of photogenerated carriers in the P_{90}-poling BLFO/BFMO is effectively suppressed [31,32]. Moreover, TRPL spectroscopy reveals that the average PL lifetime in BLFO/BFMO is longer than that of BLFO and BFMO (Fig. 3(e)). These results support the conclusion that the high photocurrent in positive-poling BLFO/BFMO is attributed to the low recombination rates [33,34]. Additionally, based on the total and partial density of states (DOS and PDOS) for BFMO, a gap state resulting from the hybridized orbital of Mn 3d and O 2p is formed due to Mn doping (Fig. 3(f)) [35]. The energy band characteristics of BLFO are similar to those of BFMO (Fig. S10 in the ESM). It is proposed that the gap state may be the cause of the high recombination in BLFO, BFMO, and as-grown BLFO/BFMO [36].

To investigate the origin of the low recombination in the positive-poling BLFO/BFMO, the surface potential of the Au/BLFO and BFMO/LNO interfaces is measured. Figure 3(g1) shows the topography of the Au/BLFO interface, where the thickness of the Au electrode is approximately 30 nm (Fig. 3(g2)). The corresponding surface potential of the as-grown state is

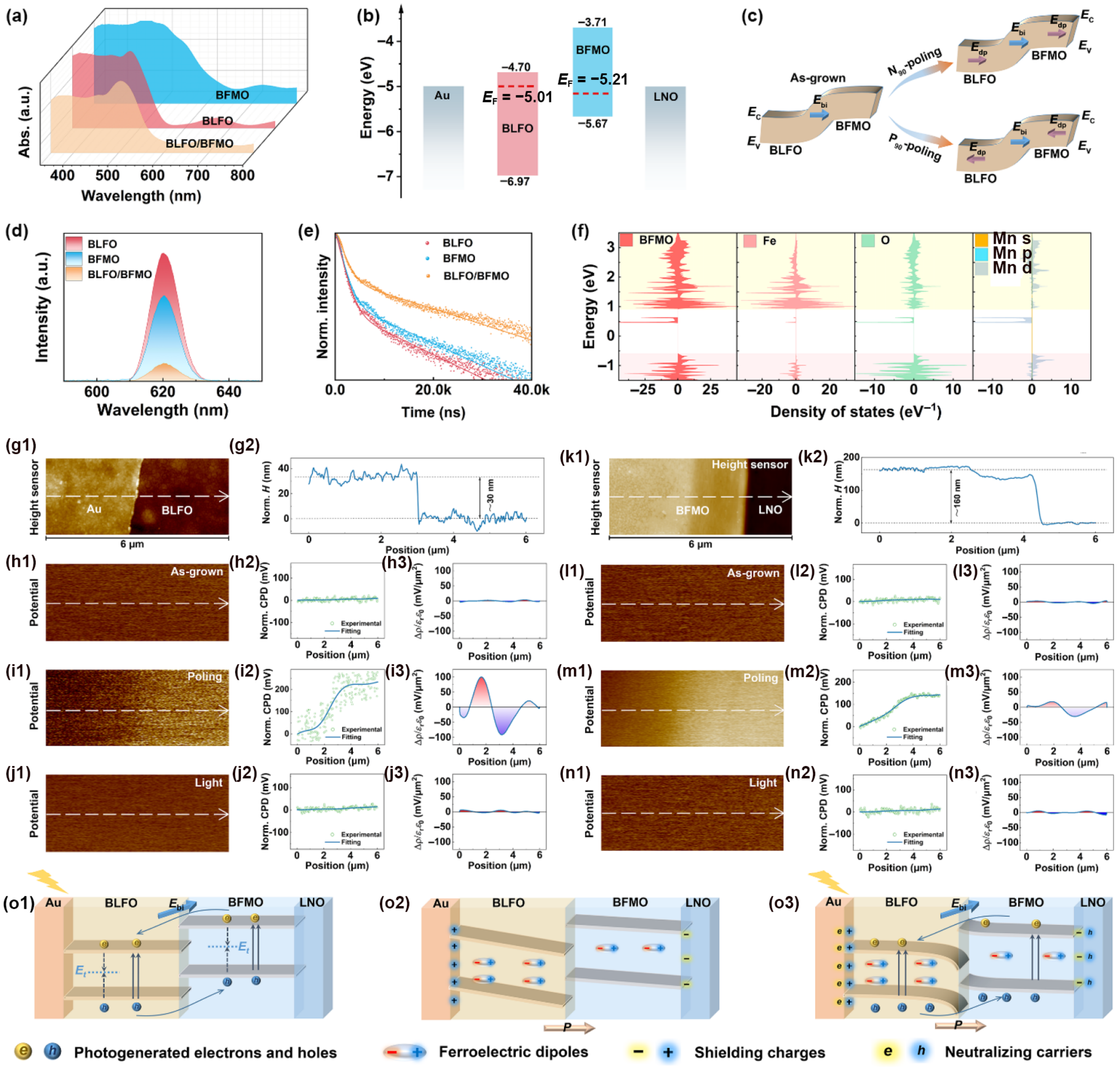

Fig. 3 (a) UV–vis absorption spectra of BLFO, BFMO, and BLFO/BFMO. (b) Energy band structure of Au/BLFO/BFMO/LNO device. (c) Schematic illustrations of driving electric field based on energy band structure. (d) PL spectra of BLFO, BFMO, and BLFO/BFMO at 412 nm excitation. (e) TRPL spectra of BLFO, BFMO, and BLFO/BFMO. (f) DOS and PDOS of BFMO perovskite. (g1) Topography of Au/BLFO interface and (g2) height profile corresponding to white arrow in (g1). Potential maps, CPD profiles corresponding to white arrow, and charge-density distribution profiles of Au/BLFO interface: (h1–h3) as-grown, (i1–i3) P_{90}-poling, and (j1–j3) illumination. (k1) Topography of BFMO/LNO interface and (k2) height profile corresponding to white arrow in (k1). Potential maps, CPD profiles corresponding to white arrow, and charge-density distribution profiles of BFMO/LNO interface: (l1–l3) as-grown, (m1–m3) P_{90}-poling, and (n1–n3) illumination. Schematic illustrations of separation and recombination for photogenerated carriers in (o1) as-grown, (o2) positive-poling, and (o3) illuminated Au/BLFO/BFMO/LNO devices.

shown in Fig. 3(h1). ACPD of approximately zero is observed between the Au and BLFO layers (Fig. 3(h2)), attributed to their similar work functions. By calculating the second derivatives of the fitting CPD in Fig. 3(h2), the charge density distribution profile is determined, as shown in Fig. 3(h3) [36,37]. Few charges are present at the as-grown Au/BLFO interface. After P_{90} poling, the CPD of the Au/BLFO interface increased (Figs. 3(i1) and 3(i2)), leading to a corresponding increase in charge density (Fig. 3(i3)). Interestingly, the CPD and charge density distribution return to the as-grown level when P_{90}-poling BLFO/BFMO is illuminated by a laser (450 nm, 100 mW), as shown in Figs. 3(j1)–3(j3). Through heating-mode KPFM measurements, it is found that 55 °C (the surface temperature of BLFO/BFMO under the illumination of 100 mW/cm^2 for 200 s) does not lead to a change in the CPD (Fig. S11 in the ESM). Therefore, the change in the surface potential of the Au/BLFO interface is just caused by the illumination rather than by the temperature elevation. Similar potential behavior is also found at the BFMO/LNO interface (Figs. 3(k)–3(n)). In contrast, the CPD of the BFMO/LNO interface is smaller than that of the Au/BLFO interface after positive poling. Meanwhile, the potential of the Au/BLFO and BFMO/LNO interfaces in N_{90}-poling BLFO/BFMO is also measured, as shown in Figs. S12(a)–S12(h) in the ESM. Due to the opposite direction of polarization, a decreasing trend in the potential is observed from Au to BLFO (Figs. S12(c1) and S12(c2) in the ESM). It is noteworthy that the CPD and charge density distribution do not change when N_{90}-poling BLFO/BFMO is illuminated (Figs. S12(d1)–S12(d3) in the ESM). The BFMO/LNO interface also exhibits the same behavior as the Au/BLFO interface (Figs. S12(e)–S12(h) in the ESM). These results indicate that ferroelectric polarization significantly influences the charge distribution at both interfaces, serving as a crucial factor in modulating the recombination of photogenerated carriers.

Energy band diagrams across the Au/BLFO/BFMO/LNO structure are schematically presented in Figs. 3(o1)–3(o3) to elucidate the behavior of photogenerated carrier recombination. According to the results in Figs. 3(b), 3(h), and 3(l), the energy band of the as-grown Au/BLFO/BFMO/LNO is depicted in Fig. 3(o1). The photogenerated electron–hole pairs in the BLFO and BFMO layers under illumination will recombine rapidly through gap-state assistance [37]. The recombination behavior is similar to that of the individual BLFO and BFMO thin films, leading to a low output photocurrent. After P_{90} poling, local free positive charges accumulate on the BLFO surface to screen the polarization of BLFO, while negative charges on the BFMO surface screen the polarization of BFMO based on a capacitance effect (Fig. 3(o2)). This leads to a warping band structure at the Au/BLFO and BFMO/LNO interfaces, as indicated by the results in Figs. 3(i3) and 3(m3). Moreover, the quantities of the positive and negative screening charges are different due to the differing polarization of the BLFO and BFMO layers, which accounts for the differing CPD observed at the Au/BLFO and BFMO/LNO interfaces (Figs. 3(i2) and 3(m2)). When the P_{90}-poling BLFO/BFMO is illuminated, the photogenerated electrons are driven by E_{bi} to neutralize the positive screening charges at the Au/BLFO interface, while the holes neutralize the negative screening charges at the BFMO/LNO interface (Fig. 3(o3)). Consequently, the CPD of the Au/BLFO and BFMO/LNO interfaces decreases, which returns to the as-grown state. The quantity variance in positive and negative screening charges causes unequal carrier compensation. This leads to an imbalance between photogenerated electrons and holes, which is highly beneficial for suppressing photogenerated carrier recombination. As a result, the unpaired photogenerated electrons and holes are driven by the E_{bi} to contribute to the photocurrent. For the N_{90}-poling BLFO/BFMO, negative and positive screen charges are formed at the Au/BLFO and BFMO/LNO interfaces, respectively, leading to the absence of neutralization between the screening charges and photogenerated electrons and holes. Therefore, it is demonstrated that the asymmetrical polarization of BLFO/BFMO significantly suppresses the recombination of electron–hole pairs, giving rise to a high output photocurrent.

3.3 Self-powered photodetection performance and applications

The high output photocurrent offers exciting prospects for self-powered photodetection. The photodetection performance of P_{90}-poling BLFO/BFMO is investigated, as shown in Fig. 4. The J_{sc} increases with increasing intensity of sunlight (Fig. 4(a)). The results reveal an approximately linear dependence between J_{sc} and the illumination intensity, indicating the photocurrent-dominated photovoltaic effect [38]. The responsivity (R) and detectivity (D^*) as the key photodetection parameters are obtained from 1 to 100 mW/cm^2, as shown in Fig. 4(b). The R and D^* can reach 0.23 A/W and 2.14×10^{12} Jones under the illumination of 1 mW/cm^2, exhibiting high photoresponse and sensitivity. The response time (τ_r and τ_d) is defined as the time required for J_{sc} to change between 10% and 90% of the maximal value [39]. The τ_r and τ_d are 6.6 and 7.5 ms under the sunlight of 100 mW/cm^2, respectively (Fig. 4(c)). In addition, the photoresponse under weak light intensity is also investigated. The response time becomes longer under weak light intensity (Fig. S13 in the ESM). This is attributed to the reduced number of photogenerated carriers under weak light, which results in a slower increase in the signal current. Figure 4(d) compares the photodetection performance of BLFO/BFMO and the individual BLFO and BFMO thin films. BLFO/BFMO possesses superior self-powered photodetection performance. Figure 4(e) shows the J_{sc} of BLFO/BFMO under the monochromatic light (0.5 mW/cm^2) of 365–675 nm. Notably, J_{sc} has a nonmonotonic change, indicating the wavelength dependence of J_{sc}. The maximum R and D^* are 0.50 A/W and 4.68×10^{12} Jones, respectively, obtained at 475 nm (Fig. 4(f)). The response time across all wavelengths is lower than 7 ms (Fig. 4(g)), indicating a fast photoresponse under monochromatic light. A comparison of R and D^* between BLFO/BFMO and other ferroelectric photodetection materials is shown in Fig. 4(h). The photodetection performance of BLFO/BFMO is markedly higher than that of BaTiO$_3$-based [40–46], Pb(Zr,Ti)O$_3$-based [47–50], BiFeO$_3$-based [51–53], Bi$_{0.5}$Na$_{0.5}$TiO$_3$-based [54], and bismuth layered perovskite [21] ferroelectric materials and heterostructures. These results indicate that BLFO/BFMO has great application potential in self-powered photodetection fields.

To demonstrate the optical communication application of the Au/BLFO/BFMO/LNO self-powered photodetector, the photoresponse is measured under both analog signal and digital signal modes. Figure 5(a) presents a schematic illustration of the optical communication system, consisting of signal input and signal output components. For analog signal communication, a continuous change in light intensity over time serves as the input signal, in which the information is encoded into Base64 code for transmission, as shown in Fig. 5(b). When a laser (405 nm) carrying the information irradiates the Au/BLFO/BFMO/LNO photodetector, the device is capable of converting the signal into a continuous short-circuit current (I_{sc}), as shown in Fig. 5(c). For instance, in this work, an encrypted character string (YnA8Fwg), corresponding to the light intensity at 25-s intervals, which are marked by blue-filled dots, serves as the input signal (Fig. 5(b)).

The curve of the I_{sc} signal exhibits a shape that closely resembles that of the input signal, and the data at intervals of 25 s marked by red-filled dots can accurately decode the communication information (YnA8Fwg, a given string of code containing both uppercase and lowercase letters and digits), as shown in Fig. 5(c). Owing to the rapid photoresponse and high sensitivity characteristics of BLFO/BFMO, it is believed that BLFO/BFMO has potential application in analog signal communication. Furthermore, in digital signal mode, a discrete form of signal consisting of binary numbers (0 or 1) is generated by the switching of light ("on" corresponding to "1"; "off" corresponding to "0"). An on/off signal of the laser, representing the information "FEPD" (the abbreviation of Ferroelectric Photodetection) based on ASCII code, is used as the input, as shown in Fig. 5(d). The Au/BLFO/BFMO/LNO photodetector can swiftly convert this light signal into an I_{sc} signal (Fig. 5(e)). The on/off signal of I_{sc} can be further decoded to reveal the information "FEPD", thereby achieving digital signal communication. Figure S14 in the ESM shows that the output signal consists of the short-circuit current corresponding to the input signal with different bit rates from 5 to 20 bps. With the increase in the bit rate, the output signal progressively weakens and becomes distorted. This is primarily because the response time of BLFO/BFMO is on the order of milliseconds, making it difficult to match higher frequencies. Movie S1 in the ESM provides a real-time demonstration of the digital signal communication process. These results highlight the potential of the Au/BLFO/BFMO/LNO self-powered photodetector with a dual-functional detection regime for an intelligent and secure communication system. To further explore the imaging application, single-pixel imaging is achieved under

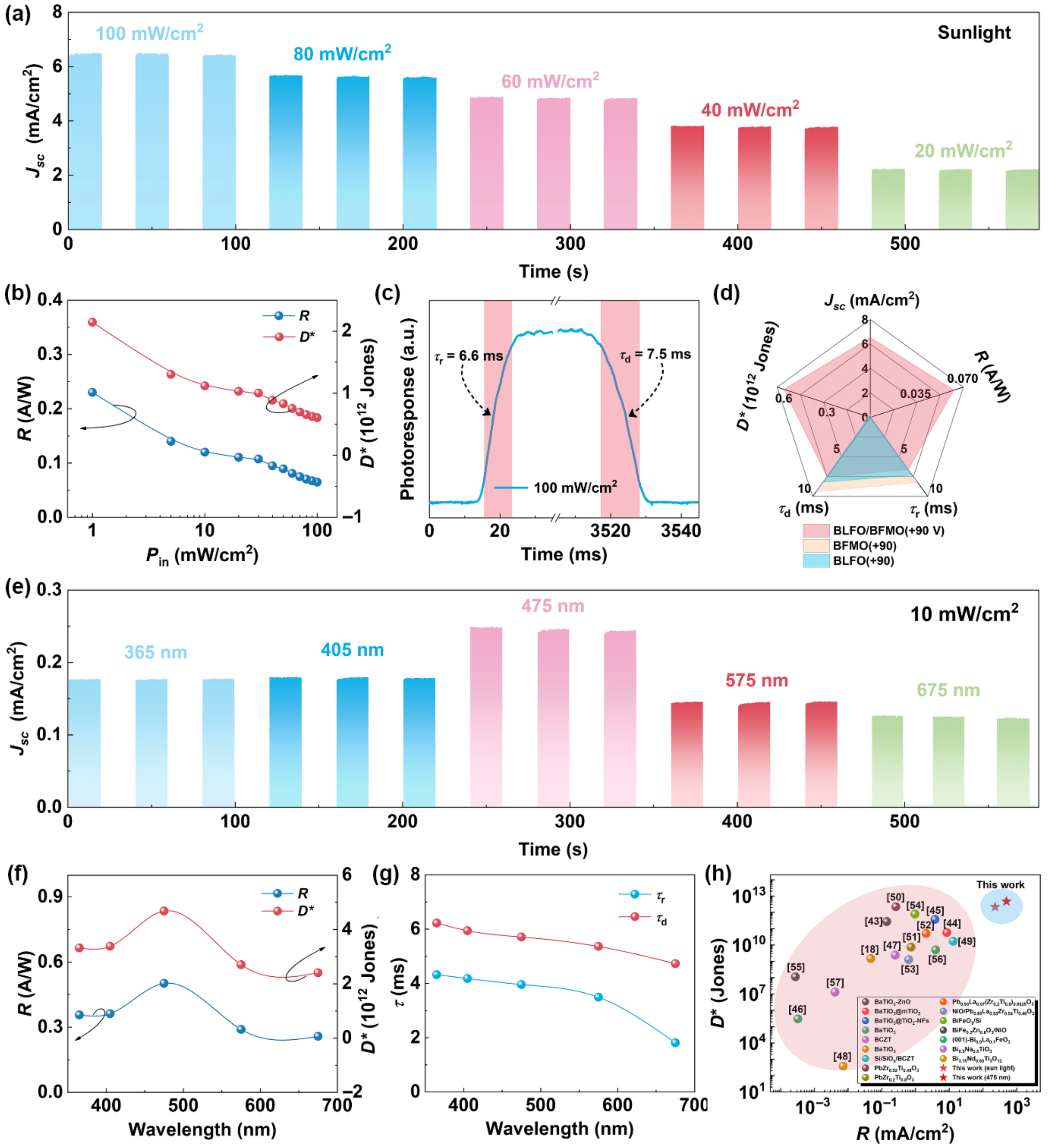

Fig. 4 (a) Time-dependent J_{sc} of BLFO/BFMO under sunlight with various power intensities. (b) R and D^* of BLFO/BFMO as a function of illumination intensity. (c) Response time of BLFO/BFMO under illumination of 100 mW/cm^2. (d) Comparison of photodetection performance between BLFO/BFMO and single-layer thin films. (e) Time-dependent J_{sc} of BLFO/BFMO under monochromatic light with various wavelengths. (f) R and D^* of BLFO/BFMO as a function of wavelength. (g) τ_r and τ_d as a function of wavelength. (h) Comparison of R and D^* between BLFO/BFMO and other ferroelectric materials.

zero bias using the laser. Figure 5(f) shows the imaging system, where a mask inscribed with a hollow "Test" is fixed to an automated two-dimensional (2D) translation stage. The 2D translation stage moves continuously along the horizontal and vertical directions, controlling whether the incident light illuminates the mask or passes through the hollow "Test" pattern to reach the photodetector. Consequently, this generates either a dark current or a photocurrent signal, depending on the light path. The photodetector generates the real-time current signal, which is recorded and subsequently converted into a high-resolution image of the word "Test", as illustrated in Fig. 5(g). These results demonstrate that the Au/BLFO/BFMO/LNO photodetector possesses excellent optical communication and imaging performance.

3.4 Optoelectronic synaptic behavior and applications

The biological synapse is a fundamental component of the biological visual system. In this work, the BLFO/BFMO heterostructure is employed to simulate an NVS. A schematic illustration of the human visual system based on the Au/BLFO/BFMO/LNO device is shown in Fig. 6(a). Synapses play a crucial role in the processes of learning and memory in the human brain. Synaptic pathways transmit and preprocess visual signals before relaying them to the visual cortex for further processing. Here, BLFO/BFMO functions as an NVS, emulating the light-sensing and synaptic functions of retinal neurons under optical stimulation. Upon activation of the presynaptic neuron, neurotransmitters are released into the synaptic cleft and bind to receptors on the postsynaptic neuron, thereby inducing an excitatory postsynaptic current (EPSC) [55]. To evaluate the short-term plasticity (STP) of BLFO/BFMO, paired-pulse facilitation (PPF) is investigated. Under a 10-V bias voltage, two consecutive 405-nm optical pulses, each with a 5-s duration and a 5-s pulse interval, are applied to BLFO/BFMO. The slow facilitation magnitude (A_2) of the second pulse is higher than the fast facilitation magnitude (A_1) of the first pulse, demonstrating enhanced synaptic plasticity (Fig. 6(b)). $(A_2–A_1)/A_1$ is defined as the PPF index [56]. Figure 6(c) shows that the PPF index decreases with increasing pulse interval. The experimental data of the PPF index can be fitted by Eq. (1) [57]:

$$\mathrm{PPF} = A_0 + A_1 \exp\left(-\frac{\Delta t}{\tau_1}\right) + A_2 \exp\left(-\frac{\Delta t}{\tau_2}\right) \tag{1}$$

where Δt is the pulse interval time, A_1 and A_2 are the fast and slow facilitation magnitudes, and τ_1 and τ_2 are the synaptic times. According to the fitted result, τ_1 and τ_2 are 0.47 and 4.54 s,

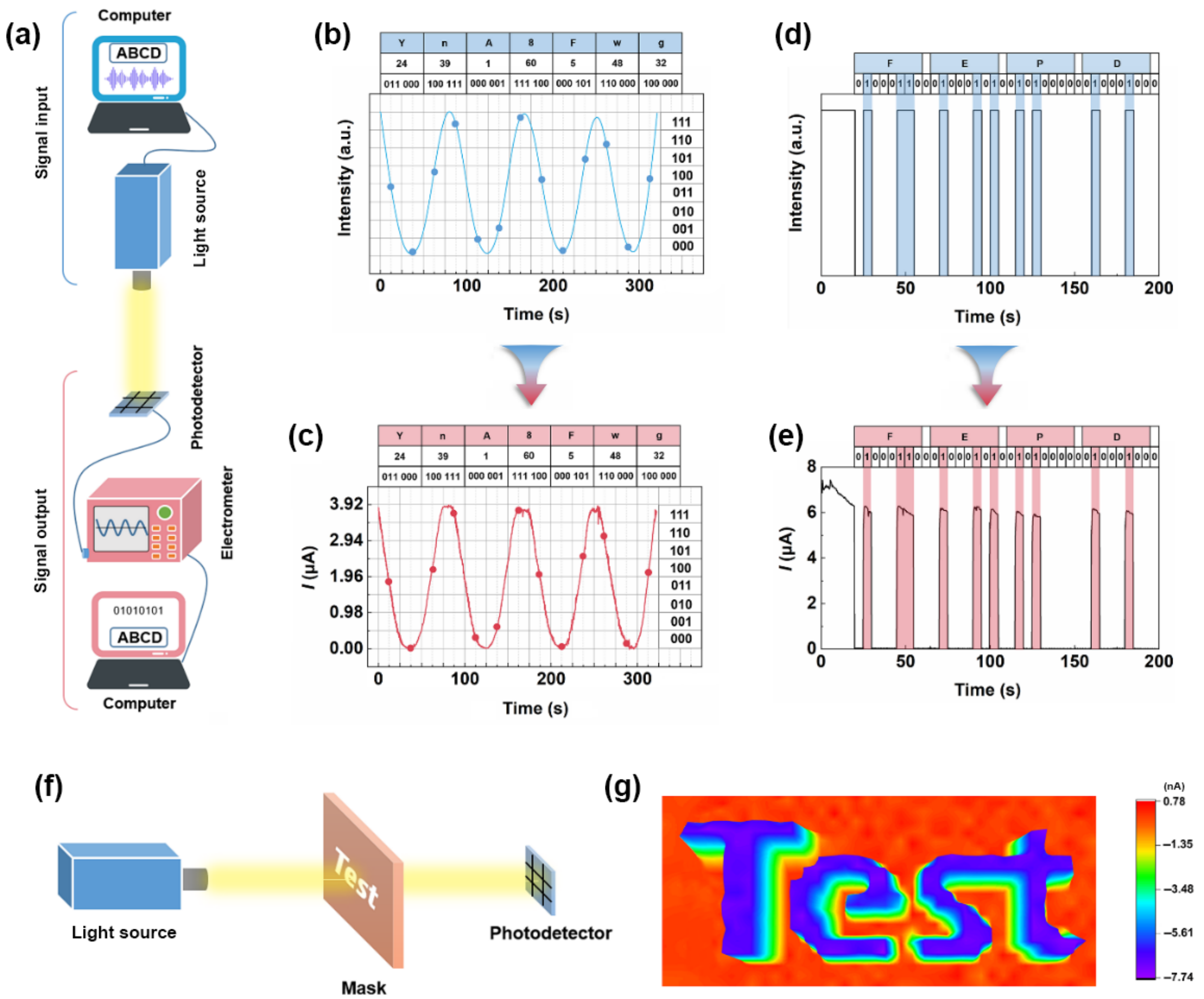

Fig. 5 (a) Schematic illustration of optical communication application of Au/BLFO/BFMO/LNO photodetector. (b) Input signal consists of continuous light intensity under analog signal mode. (c) Output signal consists of a continuous short-circuit current corresponding to Fig. 6(b). (d) Input signal consists of on/off light intensity under digital signal mode. (e) Output signal consists of a discrete short-circuit current corresponding to Fig. 6(d). (f) Schematic illustration of Au/BLFO/BFMO/LNO photodetector for imaging applications. (g) Imaging result of "Test" patterns.

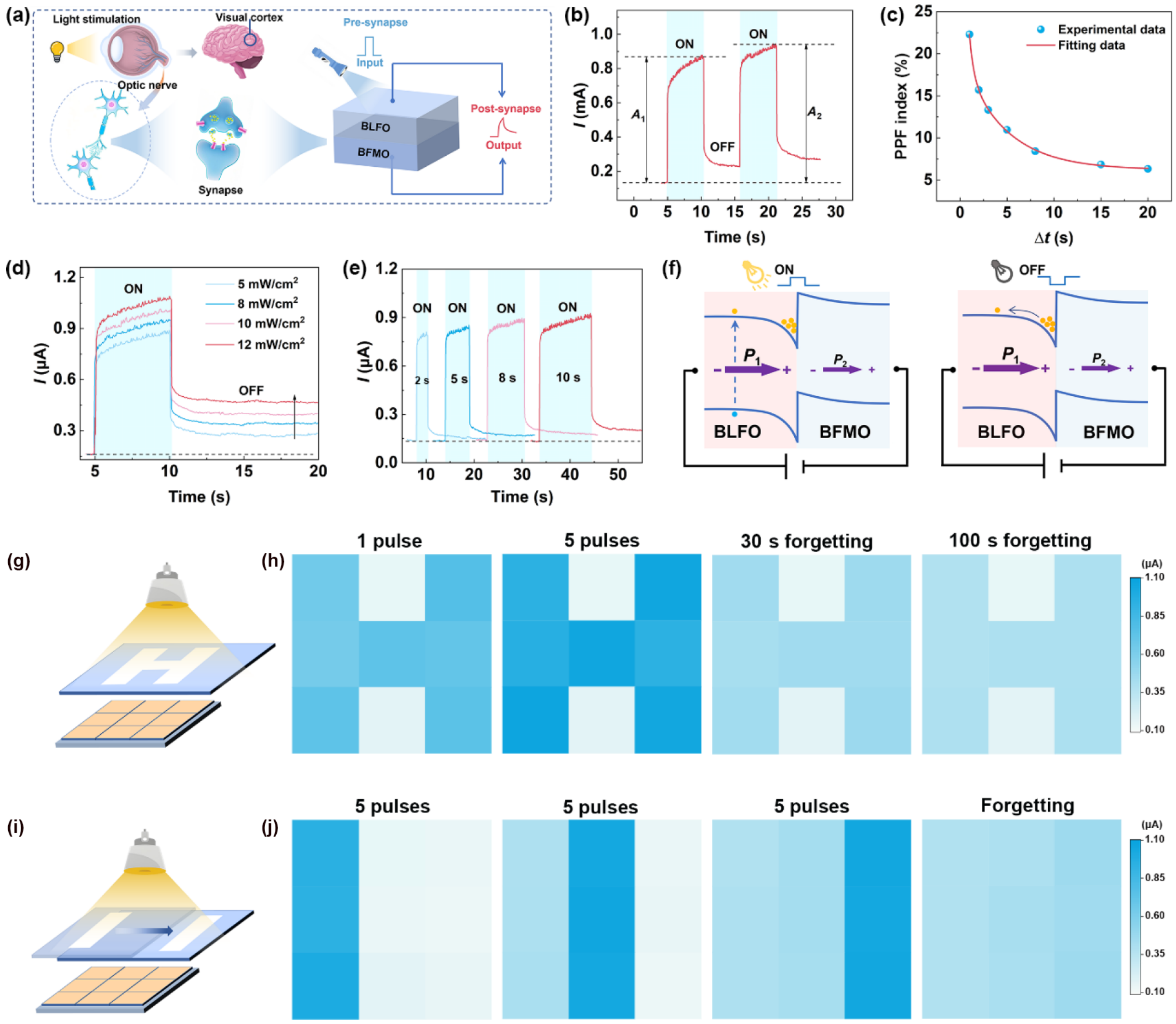

Fig. 6 (a) Schematic illustration of human visual system based on BLFO/BFMO heterostructure. (b) PPF response simulated by applying two light pulses. (c) PPF index fitting results plotted by different pulse intervals. (d) Optical response at 405 nm wavelength with different powers. (e) Optical response with different irradiation time. (f) Synapse mechanism of BLFO/BFMO heterostructure. (g) Schematic illustration of image memory function of BLFO/BFMO synaptic device array. (h) Results of image memory. (i) Schematic illustration of motion recognition function of BLFO/BFMO synaptic device array. (j) Results of motion recognition.

respectively. Figure 6(d) shows the effect of light intensity on EPSCs. With increasing light intensity, the EPSC increases. Figure 6(e) shows that increasing the pulse width enhances the EPSC. Therefore, enhanced optical stimulation, achieved by modulating both light intensity and pulse width, enables a gradual increase in current amplitude, mirroring the learning behavior observed in the human brain. As demonstrated in Fig. S15 in the ESM, repeated cycles of light switching are applied to emulate the learning–forgetting process. The results show that the EPSC of BLFO/BFMO increases after repeated learning or relearning sessions, indicating that prior acquisition significantly enhances memory retention. The observed synaptic response arises from a trap state induced by non-equilibrium polarization within BLFO/BFMO, as shown in Fig. 6(f). The applied bias induces polarization in BLFO/BFMO during this process. The polarization causes the energy bands of the BLFO layer to bend downward at the interface, while those of the BFMO layer bend upward. The non-equilibrium polarization between the BLFO and BFMO layers creates a charge imbalance at their interface. This charge imbalance, in turn, leads to the formation of an electron trap state within the more sharply bent energy bands of the BLFO layer. Under illumination, the photogenerated electron–hole pairs result in an enhanced EPSC. Some photogenerated electrons are trapped to compensate for the interfacial charge imbalance. These trapped electrons can be slowly released via thermal fluctuations or polarization variations, enabling synaptic plasticity. Capitalizing on its optoelectronic memory and synaptic properties, a 3 × 3 sensor array is fabricated based on BLFO/BFMO. The image memory function is investigated by stimulating the device through an “H”-patterned photomask with a series of optical pulses (Fig. 6(g)). The images are constructed by measuring the current from each pixel in the array (Fig. 6(h)). Increasing the number of pulses enhances the output current, leading to improved image contrast. Even at 30 and 100 s following the light pulse termination, the image can still be clearly resolved. In addition, to track the dynamic response, the “I”-patterned photomask is shifted at 5-pulse intervals, and the current is measured after each shift (Fig. 6(i)). The current mapping reveals that image “I” moves from left to right, as shown in Fig. 6(j). These results demonstrate the excellent image memory capability of BLFO/BFMO.

4 Conclusions

This work demonstrates a non-equilibrium polarization strategy in a BLFO/BFMO ferroelectric heterostructure that simultaneously achieves breakthrough photodetection performance and optoelectronic synapse functionalities. By engineering non-equilibrium polarization, we obtain a 30-fold enhancement in photocurrent density through effective carrier recombination suppression, leading to high responsivity and detectivity among ferroelectric materials. The designed heterostructure further exhibits synaptic behaviors, including short-term plasticity and learning–forgetting processes, enabled by non-equilibrium polarization-induced trap state. These dual capabilities are successfully integrated into BLFO/BFMO, which accomplishes dual-mode optical communication, high-resolution imaging, and image memory. Our findings establish a materials-design paradigm for developing multifunctional ferroelectric systems, opening a new route for integrating perception and processing within a single material.

Acknowledgements

This work was supported by the Natural Science Foundation of China (Nos. 12464001 and 12264036), the Natural Science Foundation of Inner Mongolia (Nos. 2021JQ06 and 2024MS05016), the Development Program for Innovative Research Teams in Higher Education Institutions of Inner Mongolia (No. NMGIRT2510), "Lucheng Talent" Project Innovation and Entrepreneurship Team, the Program for "Grassland Talents" of Inner Mongolia, "Light of the West" Talent Training Program of Chinese Academy of Sciences, the Talent Development Fund of Inner Mongolia, and Basic Research Funds for Universities Directly under Inner Mongolia (Nos. 2023RCTD008, 2024QNJS002, and 2024QNJS036).

Availability of data and materials

The data that support the findings of this study are available from the corresponding author upon reasonable request.

Competing interests

The authors have no competing interests to declare that are relevant to the content of this article.

Electronic Supplementary Material

Supplementary material is available in the online version of this article at https://doi.org/10.26599/JAC.2026.9221272.

References

[1] Wang SY, Chen CS, Yu ZH, *et al.* A MoS_2/PTCDA hybrid heterojunction synapse with efficient photoelectric dual modulation and versatility. *Adv Mater* 2019, **31**: 1806227.

[2] Liu X, Wang DH, Chen W, *et al.* Optoelectronic synapses with chemical-electric behaviors in gallium nitride semiconductors for biorealistic neuromorphic functionality. *Nat Commun* 2024, **15**: 7671.

[3] Liu KQ, Zhang T, Dang BJ, *et al.* An optoelectronic synapse based on α-In_2Se_3 with controllable temporal dynamics for multimode and multiscale reservoir computing. *Nat Electron* 2022, **5**: 761–773.

[4] Gao S, Liu G, Yang HL, *et al.* An oxide Schottky junction artificial optoelectronic synapse. *ACS Nano* 2019, **13**: 2634–2642.

[5] Xie PS, Huang YL, Wang W, *et al.* Ferroelectric P(VDF–TrFE) wrapped InGaAs nanowires for ultralow-power artificial synapses. *Nano Energy* 2022, **91**: 106654.

[6] Nath SK, Das SK, Nandi SK, *et al.* Optically tunable electrical oscillations in oxide-based memristors for neuromorphic computing. *Adv Mater* 2024, **36**: 2400904.

[7] Du W, Li CH, Xiao YX, *et al.* Mechanisms and applications of neuromorphic sensors for intelligent visual perception. *Sci China Mater* 2023, **66**: 4550–4565.

[8] Hu YQ, Xu W, Liu NT, *et al.* Artificial optoelectronic synapses based on light-controllable ferroelectric semiconductor memristor. *Adv Opt Mater* 2024, **12**: 2302887.

[9] Cheng SL, Fan Z, Rao JJ, *et al.* Highly controllable and silicon-compatible ferroelectric photovoltaic synapses for neuromorphic computing. *iScience* 2020, **23**: 101874.

[10] Luo ZD, Xia X, Yang MM, *et al.* Artificial optoelectronic synapses based on ferroelectric field-effect enabled 2D transition metal dichalcogenide memristive transistors. *ACS Nano* 2020, **14**: 746–754.

[11] Kim MK, Lee JS. Synergistic improvement of long-term plasticity in photonic synapses using ferroelectric polarization in hafnia-based oxide-semiconductor transistors. *Adv Mater* 2020, **32**: 1907826.

[12] Jian ZF, Li WH, Zhang L, *et al.* Ferroelectric polarization modulated optoelectronic synapses based on $BaTiO_3$/TiO_2 heterojunction for non-volatile visual memory. *J Colloid Interf Sci* 2025, **700**: 138398.

[13] Wang YR, Wang F, Wang ZX, *et al.* Reconfigurable photovoltaic effect for optoelectronic artificial synapse based on ferroelectric p–n junction. *Nano Res* 2021, **14**: 4328–4335.

[14] Kang SJ, Jung W, Gwon OH, *et al.* Photo-assisted ferroelectric domain control for α-In_2Se_3 artificial synapses inspired by spontaneous internal electric fields. *Small* 2024, **20**: 2307346.

[15] Yan SA, Zang JY, Xu P, *et al.* Recent progress in ferroelectric synapses and their applications. *Sci China Mater* 2023, **66**: 877–894.

[16] Hu YQ, Zhu YX, Chen XL, *et al.* Ferroelectric-based optoelectronic synapses for visual perception: From materials to systems. *Nanomaterials* 2025, **15**: 863.

[17] Guo F, Song ML, Wong MC, *et al.* Multifunctional optoelectronic synapse based on ferroelectric van der Waals heterostructure for emulating the entire human visual system. *Adv Funct Mater* 2022, **32**: 2108014.

[18] Ji RX, Feng GD, Jiang CL, *et al.* Fully light-modulated organic artificial synapse with the assistance of ferroelectric polarization. *Adv Electron Mater* 2022, **8**: 2101402.

[19] Jiang YR, Zhang LL, Wang R, *et al.* Asymmetric ferroelectric-gated two-dimensional transistor integrating self-rectifying photoelectric memory and artificial synapse. *ACS Nano* 2022, **16**: 11218–11226.

[20] Wu YB, Wang XP, Tian G, *et al.* Inverse design of ferroelectric-order in perovskite crystal for self-powered ultraviolet photodetection. *Adv Mater* 2022, **34**: 2105108.

[21] Chen J, Mao JX, Wang ZH, *et al.* Bandgap narrowing and polarization enhancement in (K,Na,Li)(Nb,Sb,Ta)O_3+x% Fe_2O_3 lead-free ceramics for photovoltaic applications. *J Adv Ceram* 2023, **12**: 1406–1417.

[22] Tian MW, Liu XJ, Gong A, *et al.* Efficient ultraviolet–visible-near infrared self-powered photodetector based on hexagonal $YMnO_3$-based ferroelectric thin film by multiscale polarity structure optimization. *Chem Eng J* 2023, **452**: 139040.

[23] Chen ZB, Lin XQ, Lin SX, *et al.* Inverted-structural self-powered Gan /PZT/ITO UV photodetector enhanced by ferroelectric modulation. *Adv Electron Mater* 2024, **10**: 2300588.

[24] Li Z, Zhao Y, Li WL, *et al.* A self-powered flexible UV–visible photodetector with high photosensitivity based on $BiFeO_3$/$XTiO_3$ (Sr, Zn,Pb) multilayer films. *J Mater Chem A* 2022, **10**: 8772–8783.

[25] Zhong WM, Tang XG, Liu QX, *et al.* Artificial optoelectronic synaptic characteristics of Bi_2FeMnO_6 ferroelectric memristor for neuromorphic computing. *Mater Design* 2022, **222**: 111046.

[26] Yuan YB, Xiao ZG, Yang B, *et al.* Arising applications of ferroelectric materials in photovoltaic devices. *J Mater Chem A* 2014, **2**: 6027–6041.

[27] Han X, Ji Y, Yang Y. Ferroelectric photovoltaic materials and devices. *Adv Funct Mater* 2022, **32**: 2109625.

[28] Zhang GC, Dai JQ, Zhu XJ, *et al.* Tuning leakage current and ferroelectric properties in spin-coated $BiFeO_3$ films through Cr doping and post-annealing atmosphere control. *Mater Today Chem* 2024, **42**: 102423.

[29] Li Y, Wang GC, Gong A, *et al.* High-performance ferroelectric electromagnetic attenuation materials with multiple polar units based on nanodomain engineering. *Small* 2022, **18**: 2106302.

[30] Yang YB, Mao HC, Wang J, *et al.* Large switchable photoconduction within 2D potential well of a layered ferroelectric heterostructure. *Adv Mater* 2020, **32**: 2003033.

[31] Zhang CC, Wang ZK, Yuan S, *et al.* Polarized ferroelectric polymers for high-performance perovskite solar cells. *Adv Mater* 2019, **31**: 1902222.

[32] Guo JJ, Meng RT, Liu Y, *et al.* Ferroelectric $BaTiO_3$ nanoparticles embedded at the p–n heterojunction interface improves the carrier transport in kesterite solar cells. *Adv Funct Mater* 2024, **34**: 2316119.

[33] Hou Y, Aydin E, De Bastiani M, *et al.* Efficient tandem solar cells with solution-processed perovskite on textured crystalline silicon. *Science* 2020, **367**: 1135–1140.

[34] Li SY, Zhang Y, Yang W, *et al.* 2D perovskite $Sr_2Nb_3O_{10}$ for high-performance UV photodetectors. *Adv Mater* 2020, **32**: 1905443.

[35] Matsuo H, Noguchi Y, Miyayama M. Gap-state engineering of visible-light-active ferroelectrics for photovoltaic applications. *Nat Commun* 2017, **8**: 207.

[36] Tan S, Huang TY, Yavuz I, *et al.* Stability-limiting heterointerfaces of perovskite photovoltaics. *Nature* 2022, **605**: 268–273.

[37] Min LL, Sun HX, Guo LQ, *et al.* Frequency-selective perovskite photodetector for anti-interference optical communications. *Nat Commun* 2024, **15**: 2066.

[38] Luo P, Wang FK, Qu JY, *et al.* Self-driven WSe_2/Bi_2O_2Se van der Waals heterostructure photodetectors with high light on/off ratio and fast response. *Adv Funct Mater* 2021, **31**: 2008351.

[39] Ma SP, Li GH, Li Z, *et al.* Negative photoconductivity of Fe_3GeTe_2 crystal with native heterostructure for ultraviolet to terahertz ultra-broadband photodetection. *Adv Mater* 2024, **36**: 2305709.

[40] Zhang Y, Zhao XY, Chen JX, *et al.* Self-polarized $BaTiO_3$ for greatly enhanced performance of ZnO UV photodetector by regulating the distribution of electron concentration. *Adv Funct Mater* 2020, **30**: 1907650.

[41] Su L, Li ZQ, Cao F, *et al.* Tailoring the interface assembly of mesoporous TiO_2 on BTO film toward high-performance UV photodetectors. *J Mater Chem C* 2022, **10**: 9035–9043.

[42] Su L, Yan TT, Liu XY, *et al.* A tunable polarization field for enhanced performance of flexible $BaTiO_3$@TiO_2 nanofiber photodetector by suppressing dark current to pA level. *Adv Funct Mater* 2023, **33**: 2214533.

[43] Ma N, Zhang KW, Yang Y. Photovoltaic–pyroelectric coupled effect induced electricity for self-powered photodetector system. *Adv Mater* 2017, **29**: 1703694.

[44] Swain AB, Rath M, Biswas PP, *et al.* Polarization controlled photovoltaic and self-powered photodetector characteristics in Pb-free ferroelectric thin film. *APL Mater* 2019, **7**: 011106.

[45] Zhao K, Ouyang BS, Yang Y. Enhancing photocurrent of radially polarized ferroelectric $BaTiO_3$ materials by ferro–pyro–phototronic effect. *iScience* 2018, **3**: 208–216.

[46] Silva JPB, Gwozdz K, Marques LS, *et al.* Large ferro-pyro-phototronic effect in $0.5Ba(Zr_{0.2}Ti_{0.8})O_3$–$0.5(Ba_{0.7}Ca_{0.3})TiO_3$ thin films integrated on silicon for photodetection. *Carbon Energy* 2023, **5**: e297.

[47] Shen XM, Wu ZC, Lu WD, *et al.* Improved self-powered photodetection of ferroelectric $PbZr_{0.52}Ti_{0.48}O_3$ thin films via interfacial engineering. *J Phys Chem C* 2022, **126**: 18617–18622.

[48] Han ZK, Luo BC, Wang SH, *et al.* Ferroelectrically modulated and enhanced photoresponse of a Ag/PZT/NSTO self-powered photodetector in the ultraviolet range. *J Mater Chem C* 2024, **12**: 3708–3714.

[49] Zhang Y, Chen J, Cai YX, *et al.* Depolarization electric field and poling voltage-modulated $Pb,La(Zr,Ti)O_3$-based self-powered ultraviolet photodetectors. *J Am Ceram Soc* 2021, **104**: 928–935.

[50] Chen J, You D, Zhang Y, *et al.* Highly sensitive and tunable self-powered UV photodetectors driven jointly by p–n junction and ferroelectric polarization. *ACS Appl Mater Inter* 2020, **12**: 53957–53965.

[51] Lei L, Liu L, Lu XM, *et al.* Broadband and high-sensitivity photodetector based on $BiFeO_3$/Si heterojunction. *Adv Opt Mater* 2023, **11**: 2201893.

[52] Ma S, Sha ZZ, Xia FJ, *et al.* Boosting the photoresponse speed of visible-light-active bismuth ferrite thin films based on Fe-site substitution strategy and favorable heterostructure design. *Appl Surf Sci* 2022, **590**: 153054.

[53] Wang GC, Gong A, Zhang S, *et al.* High performance self-powered photodetector based on ferroelectric (001)-oriented $Bi_{0.9}La_{0.1}FeO_3$ thin film. *Thin Solid Films* 2022, **754**: 139289.

[54] Liu Y, Ji Y, Xia YL, *et al.* Enhanced photocurrent in ferroelectric $Bi_{0.5}Na_{0.5}TiO_3$ materials via Ferro–pyro–phototronic effect. *Nano Energy* 2022, **98**: 107312.

[55] Xi ZY, Liu MS, Zhang JH, *et al.* Retina-like neuromorphic visual sensor for sensing broad-spectrum ultraviolet light. *Adv Opt Mater* 2024, **12**: 2402193.

[56] Deng W, Zhang XJ, Jia RF, *et al.* Organic molecular crystal-based photosynaptic devices for an artificial visual-perception system. *NPG Asia Mater* 2019, **11**: 77.

[57] Cui DS, Pei MJ, Lin ZH, *et al.* Versatile optoelectronic memristor based on wide-bandgap Ga_2O_3 for artificial synapses and neuromorphic computing. *Light—Sci Appl* 2025, **14**: 161.